Arabian Journal of Geosciences (2020) 13: 324
https://doi.org/10.1007/s12517-020-05303-z

ORIGINAL PAPER

Acoustic emission investigation on scale effect and anisotropy of jointed rock mass by the discrete element method

Zhaohui Chong[1,2] · Qiangling Yao[1] · Xuehua Li[1] · Karekal Shivakumar[2]

Received: 25 September 2018 / Accepted: 31 March 2020 / Published online: 19 April 2020

Abstract

We investigate herein the scale effect and anisotropy of jointed rock mass (JRM) from the perspective of acoustic emission (AE) characteristics and estimate the size of the representative element volume (REV). First, we propose an AE calculation based on the discrete element method (DEM) and use the statistical results of joint planes to generate a discrete fracture network. Next, we calibrate the micro-parameters of the rock matrix and the joint plane based on physical experiment and the single plane of weakness theory, respectively. Finally, we use the proposed model to numerically simulate the AE characteristics of a JRM and estimate the size of the REV. The use of different model sizes and layer orientations shows that the AE event magnitude follows a power-law distribution. The frequency of AE events with different magnitudes follows a normal distribution, and a negative exponential relationship is found between the frequency of AE events and the number of cracks associated with each AE event. When the model size exceeds 10×10 m, the parameters of AE events (accumulated frequency, magnitude, frequency of AE events associated with only one crack, frequency of AE events associated with over ten cracks, and maximum crack number associated with each AE event) remain essentially constant. This means that the size of the REV is 10×10 m. The proposed model should also prove useful for further research into the fracture mechanism of JRM.

Keywords Representative element volume (REV) · Discrete fracture network · AE events · Moment tensor · AE magnitude

Introduction

In many civil and mining engineering projects, intact rock blocks are segmented into natural rock masses by exploiting different types of discontinuities, such as bedding planes, joints, fissures, cracks, faults, and shear zones (Younessi and Rasouli 2010; Moriya et al. 2015). Such discontinuities can seriously affect the mechanical properties of the rock mass and lead to the effect of scale and anisotropy (Kulatilake 1985; Kulatilake et al. 1993α; Gao et al. 2014; Hou et al. 2016). When the scale of a jointed rock mass (JRM) increases to a certain point, its mechanical behavior ceases to change in time. This threshold scale of a JRM is called the "representative element volume" (REV) (Min et al. 2004; Blum et al. 2007; Esmaieli et al. 2010) and can be regarded as a quantitative criterion for selecting the proper parameters with equivalent continuum methods (Wu and Kulatilake 2012). It is thus important to investigate the effect of scale and anisotropy of a JRM to estimate the size of the REV.

Considerable research has been devoted to developing procedures for characterizing the strength and deformability of a JRM, with the result being two major research methods that may be broadly described as qualitative and quantitative analysis methods. The qualitative analysis methods may be subdivided into an empirical method and a theoretical method of analysis (Zhang 2010; Karakul and Ulusay 2013; Vásárhelyi and Kovács 2017), each of which has its own strengths and weaknesses. The empirical method lacks an accurate basis for constructing a constitutive model, whereas the theoretical method is handicapped because it is impossible to obtain closed-form solutions when rock masses contain abundant pre-existing bedding planes (although fracture mechanics can be used to research rock masses containing several joint

Responsible Editor: Zeynal Abiddin Erguler

✉ Qiangling Yao
yaoqiangling@cumt.edu.cn

[1] Key Laboratory of Deep Coal Resource, Ministry of Education of China, School of Mines, China University of Mining and Technology, Xuzhou 221116, Jiangsu, China

[2] Faculty of Engineering and Information Sciences, University of Wollongong, Wollongong 2522, Australia

planes). The quantitative analysis method mainly consists of laboratory experiments and in situ tests (Kulatilake et al. 2001; Mehranpour and Kulatilake 2016; Mahdevari and Maarefvand 2016; Shi et al. 2016). Although the mechanical parameters obtained in the laboratory are not equivalent to the results obtained from in situ tests, the latter is time-consuming. More importantly, in situ tests have difficulty detecting the development of hidden cracks within a rock mass (Karacan 2009).

To obtain within a rock mass the initiation, propagation, and coalescence of cracks that are difficult to detect in the laboratory and on the in situ scale, acoustic emission (AE) instruments or micro-seismographs are widely used to detect the signals emitted when cracks are generated (Shukla et al. 2013; Zhao et al. 2014; Huang et al. 2016). AE technology was developed from the acoustic phenomenon captured by Kaiser in tensile tests (Hoek et al. 1995). Cai et al. (2007) studied AE signals released from large-scale underground excavations by using FLAC/PFC coupled with numerical simulations. AE events have been analyzed in this way to investigate the threshold of rock failure and to locate cracks within the rock mass (Xue et al. 2014).

With the development of computing techniques, ever more numerical simulations have been used to study the mechanical properties of JRM from the perspective of AE characteristics. Analog AE signals are required since they cannot be obtained directly from the mechanical properties in numerical simulation (Zhao et al. 2015). Lisjak et al. (2013) combined the finite and discrete element methods (FEM and DEM) to simulate micro-seismic events and described the crack development process in terms of three factors: the D value, AE rate, and b value. Heinze et al. (2015) put forward a poro-elasto-plastic continuum model, which quantitatively divided the rock failure process into three stages, including pre-failure stage, crack initiation stage, and macroscopic failure initiation stage. Tang et al. (2000α, β) evaluated the strength and failure process of rock mass and introduced AE events into the rock failure process analysis (RFPA). These studies had difficulty simulating randomly distributed pre-existing joints within the rock mass, and even more difficulty investigating the effect of scale and the anisotropy of a JRM. Ivars et al. (2011) investigated how scale affects the mechanical properties of rock mass based on modeling synthetic rock mass. In the particle flow code (PFC), the rock matrix is represented by a bonded particle assembly, pre-existing joints are represented by the smooth joint model (SJM), and crack initiation when the contact force exceeds the bond strength is considered analogous to AE.

In this paper, we propose a calculation that considers pre-existing joints and that can predict AE events. A third-party program is then used to calculate the moment tensor to get the magnitude of AE events. In addition, we propose a spatiotemporal principle to estimate the same AE event. The micro-parameters of the DEM model are calibrated based on confining pressure tests on intact specimens and the single plane of weakness theory. Finally, we estimate the size of the REV by investigating the effect of scale and anisotropy of JRM from the perspective of AE characteristics.

Methodology

Discrete fracture network model

The simulations were done by using the PFC, which is a two-dimensional numerical program based on the DEM. The PFC treats the discrete fracture network (DFN) model as two models, one representing the rock matrix, and the other representing the joints within the rock matrix.

In the PFC, the contact bond model, parallel bond model (PBM), and flat-joint model are three existing micro-bond models for representing a rock matrix (Cho et al. 2007; Mehranpour et al. 2018). In the contact bond model, the force in question can only be transmitted through the contact bonds between particles whereas, in the PBM, both force and torque can be transmitted through parallel bonds between particles. With the PBM, parallel bonds may be considered a group of elastic springs normally distributed over the cross section of the contact plane with the contact point as their surrounding center; these springs have a constant normal and shear stiffness and act in parallel with the point-contact springs that are used to model particle stiffness at a point (Potyondy and Cundall 2004). Because of the stiffness of the parallel bond, the relative displacement between the two particles induces a force and force moment. In addition, the macro-stiffness decreases immediately once the bond breaks in the PBM because the macro-stiffness is composed of both contact and bond stiffness. The PBM and flat-joint model can also mimic a finite-length interface between the particle contacts. In addition, there are some respective characteristics in these two models (Wu and Xu 2016). The failure model of flat-joint model cannot agree with physical experiment well. In this study, the PBM is selected in the rock matrix because it can simulate the rock in a more authentic manner.

In both the normal and the shear direction, the contact force and displacement between particles are determined by the normal stiffness $\overline{k}^n$ and shear stiffness $\overline{k}^s$ (Chen and Konietzky 2014).

In previous work, joints were usually simulated by removing particles in certain positions, which would introduce an inherent roughness between particles that would lead to an unrealistic growth of shear strength and dilation along the joint plane in the process of shearing. This weakness can be overcome, however, by using the SJM to simulate the pre-existing joint plane in the rock mass (Kulatilake et al. 2001).

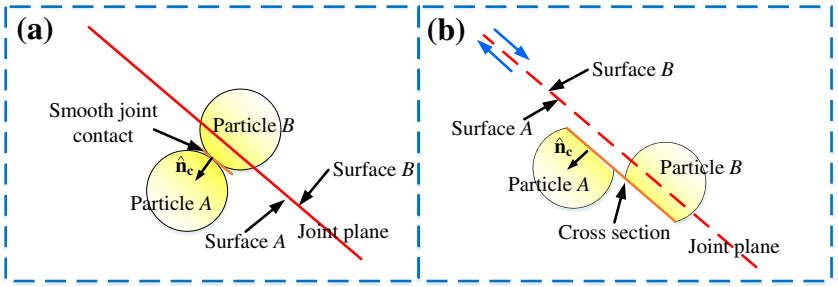

Fig. 1 Smooth joint (SJ) contact model in two dimensions (after Pierce et al. 2007): **a** typical joint plane defined; **b** joint plane closed

Figure 1 shows a typical smooth joint (SJ). Once a joint plane is defined, a SJ is assigned at the contact between particles with its center located on the opposite side of the defined joint plane (Fig. 1a). The original contacts are then removed at the contacts between particles and the SJ is redefined along the joint plane regardless of the original contact orientation. Mutual overlapping or passing through may occur between two particles having such contacts (Fig. 1b). These contacts move in accordance with the SJM laws (Pierce et al. 2007).

Acoustic emission simulation theory

The energy released after the bond rupture between neighboring particles is essentially uniform between all particle pairs because the energy magnitudes released by particle rupture in the DFN model are the same (Hazzard and Young 2000). Regarding each bond rupture as an AE event does not comply with the real micro-seismic and AE conditions in physical experiments, which means that the rupture of bonds under similar spatial and temporal conditions may be regarded as AE events. If an AE event is associated with only one crack, the contact point before rupture is regarded as its centroid. However, if the AE event is associated with more than one crack, the geometric center of these cracks is considered to be the centroid of the AE event.

The particles at the two ends of a newly generated micro-crack are defined as the source particles (particles *A* and *B*). Only cracks in direct contact with the source particles may belong to the same AE event (Fig. 2a). In the DFN model, the force is transmitted to other particles through the source particles. The magnitude and affected area of the AE event expand together with the propagation and coalescence of the cracks.

Figure 2b defines the same AE event in terms of excitation time. The excitation time for crack 1 to propagate to the border of its affected area is assumed to be T_1. The moment tensor is updated and recalculated at each time step within T_1. If no new crack is initiated within T_1, or in the affected area of crack 1, this AE event consists of only one crack and the total excitation time of the AE event is T_1. If there is a new crack (namely, crack 2) within T_1 and in the affected area of crack 1, then the affected areas of cracks 1 and 2 overlap with each other and the total excitation time of the AE event is T_0 (the excitation time for crack 2 to propagate to the border of its affected area is assumed to be T_2). Similarly, if a new crack (crack 3) initiates within T_0, the magnitude and the affected area of cracks 2 and 3 also overlap, and so on. In Fig. 2b, the total affected area of the AE event is the overlapped area of cracks 1–3 and the total excitation time is T_0, but cracks 4 and 1 do not belong to the same AE event because crack 4 is initiated after T_0 (although within the affected area of crack 1). Neither crack 5 nor crack 1 belongs to the same AE event because crack 5 does not initiate in the affected area of crack 1 (although it initiates within T_0).

The moment tensor is an important instrument widely used for quantitative measurements of micro-seismic sources (Liu et al. 2015). In the DFN model, the force and displacement of the particles can be directly obtained, which facilitates the

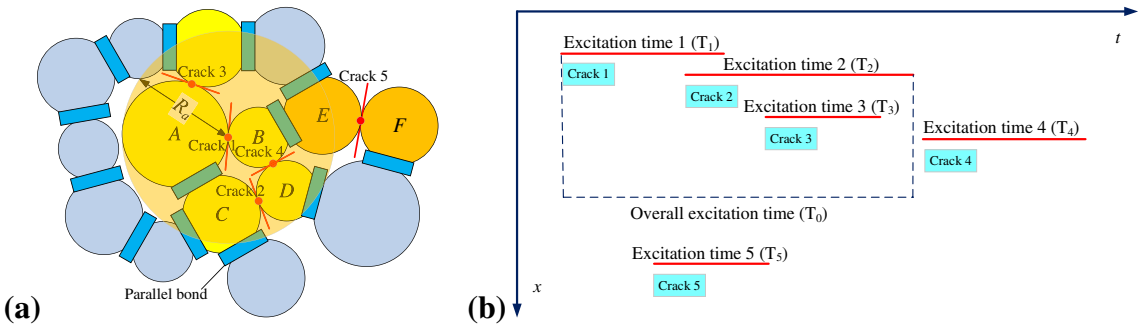

Fig. 2 Definition of same AE event in terms of **a** space and **b** time; the occurrence order of micro-cracks is crack 1, 5, 2, 3, and 4, in which cracks 1–3 belong to the same AE event

calculation of the moment tensor based on the change in contact force between particles caused by the initiation of new cracks. The moment tensor in the arithmetic model can be obtained by multiplying the change in the contact force by its corresponding leverage arm (distance from contact point to the middle point of the crack):

$$M_{ij} = \sum_{S} \left(\Delta F_i L_j\right) \tag{1}$$

where M_{ij} is the scalar seismic moment in the calculation, and ΔF_i and L_j are the nth component of the contact force and the corresponding leverage arm.

The maximum scalar moment of the moment tensor is (Lisjak et al. 2013):

$$M_0 = \sqrt{\frac{\sum_{j=1}^{i} M_{ij}^2}{2}} \tag{2}$$

where M_0 is the scalar seismic moment.

The magnitude of the AE event can be calculated by using (Heinze et al. 2015):

$$M = \frac{2}{3}\lg(M_0) - 6 \tag{3}$$

where M is the magnitude of AE events.

Calibration of numerical model

Calibration of intact rock specimens

The micro-parameters of the model related to particle contacts must be calibrated (Kulatilake et al. 1996; Kulatilake et al. 1993β). The rock materials used in this study were argillaceous sandstone from the Shanxi Formation in Shanxi Province, China. In this study, besides the uniaxial compressive strength (UCS) and Young's modulus, the cohesion c and internal friction angle ϕ obtained from physical experiments were also used in the calibration of the micro-parameters. In confining pressure tests, these two parameters can be calculated by using (Kovari et al. 1983):

$$\phi = \arcsin\frac{k-1}{k+1} \tag{4}$$

$$c = b\frac{1-\sin\phi}{2\cos\phi} \tag{5}$$

where k and b are the gradient of the fitting curve and the y intercept, respectively.

In this study, all specimens of argillaceous sandstone were processed into $\Phi 50 \times 100$ mm cylinders with each end sanded parallel to the loading system. Table 1 gives the mechanical properties of argillaceous sandstone at different confining pressure. The micro-parameters of the intact rock specimen were calibrated through trial and error. According to the results of physical experiments, Young's modulus varies little under different confining pressures, which means that Young's modulus for the intact rock specimen was calibrated before its strength parameters (including cohesion and internal friction angle).

Figure 3 plots the results of laboratory tests against simulation results under compression tests with 0.5, 2.0, 4.0, and 6.0 MPa confining pressure. The comparison between the results of the physical experiment and that of the numerical simulation shows that the proposed model reproduces the linear elastic stage, Young's modulus, and peak stress. Table 2 gives the calibrated micro-parameters of the rock matrix.

Statistics of discrete fracture network

A complicated distribution of joints in rock mass often results in nonlinear, discontinuous, and anisotropic characteristics, which means that the distribution of the joint must be understood before determining its micro-parameters. In this study, the joint distribution is explored using samples from Shanxi, China (taken from the same site where the specimens for the physical experiment were obtained).

A joint is a type of pre-existing flaw in a rock mass, and an understanding of the distribution of the joints helps to simulate the mechanical behavior and AE characteristic of the JRM. The joint distribution of the rock mass in a certain region can be obtained from regional geological surveys. In this study, we used grayscale image-processing technology (Andrä et al. 2013) to explore the joint distribution in the rock mass. The real size of the rock is approximately 7.5×10 m^2, and the image resolution is sufficient to identify the joints within the rock. According to the statistical results of the joint distribution, including joint density, dip angle, trace length, and spacing, three sets of joints exist in the rock mass. Stochastic models are effective tools for representing DFN based on the available structural data (Kulatilake et al. 2003). Table 3 lists the geometrical parameters of the joints, where type I represents the stochastic model of a negative exponential distribution of joints, type II is for a normal distribution, type III is for a logarithmic normal distribution, and type IV is for a uniform distribution.

In the PFC, the "DFN template" instruction can be used to create an independent sub-program according to the statistical properties of discontinuities (i.e., dip angle, trace length, and spacing). In this paper, three sets of joints were separately named, and each set was embedded into the DEM model according to the statistical properties given in Table 3. Finally, the DFN model was generated.

Table 1 Mechanical properties of argillaceous sandstone used in this research

Specimen number	Confining pressure (MPa)	Deviatoric stress (MPa)	Young's modulus (GPa)	Poisson's ratio	Cohesion (MPa)	Internal friction angle (°)
I-1	0.5	19.55	20.11	0.194	6.13	19.36
I-2	2.0	20.97	20.64	0.204		
I-3	4.0	24.60	22.16	0.224		
I-4	6.0	29.08	21.88	0.201		

Determination of smooth joint parameters

Up to now, no specific method has been proposed to determine the joint parameters in a DFN model. Fan et al. (2015) represented a SJ by reducing the mechanical properties of specified sections. The parameters of the SJ were determined by comparing the simulation results for specimens with non-persistent open joints with the results obtained from physical experiments under uniaxial compressive tests. Bahaaddini et al. (2013) determined the normal stiffness of the SJ ($\overline{k}_{nj}$) by simulating normal deformability tests, and the shear stiffness of SJs ($\overline{k}_{sj}$) and the friction coefficient μ_j by simulating direct shear tests. Yang and Qiao (2018) adopted a similar method to determine the parameters of SJs. Wang et al. (2016) used a sensitivity analysis to calibrate the SJ parameters of specimens with different layer orientations.

According to our previous work (Chong et al. 2017), the SJ parameters strongly affect the specimens. The peak strength of a specimen is mainly determined by the strength of the SJ, including tensile strength and cohesion. The number of cracks is affected by the ratio of the tensile strength to cohesion, which, in turn, modifies the specimen failure mode. In addition, the normal stiffness and shear stiffness exert a varying effect on the peak stress and Young's modulus of the specimen.

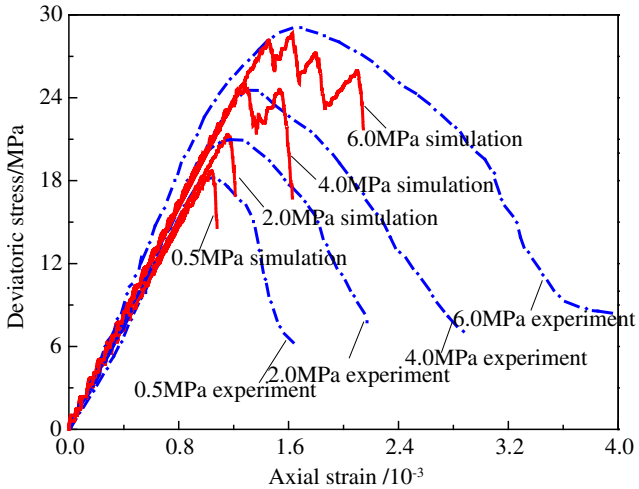

Fig. 3 Comparison between experimental and numerical deviatoric stress versus vertical strain curves

SJ micro-parameters in a large rock mass can be estimated according to previous work (Pierce et al. 2007). In the present study, three sets of SJs were assumed to be cohesionless, and their internal friction angles were assumed to be 30° and dilation angles to be 0° (Esmaieli et al. 2010). Initially, the same values were assigned to $\overline{k}_{nj}$ and $\overline{k}_{sj}$, and then the SJ micro-parameters were determined according to the single plane of weakness theory (Jaeger 1960α, β; Mclamore and Gray 1967). Further trial and error tests were done to calibrate the micro-parameters of the SJ. Figure 4 compares the result of a numerical simulation with a result calculated based on the single plane of weakness theory when the specimen has a single joint plane. The comparison reveals that the selected SJ micro-parameters in Table 4 are the best for this research. The direct shear test using the PFC^{2D} can also be used to calibrate the SJ micro-parameters (Mehranpour and Kulatilake 2017).

Model setup

Based on the calibrated DEM model from above, a series of numerical simulations was run to investigate the effect of scale and anisotropy on a JRM and to estimate the size of the REV. Figure 5 shows a schematic diagram of the study. The angle in the vertical direction is assumed to be $\theta = 0°$, where θ rotates clockwise in 30° steps. In this way, the properties of the JRM were analyzed and the size of the REV was determined in terms of the AE characteristics. In this study, the DEM models with 15 different sizes (i.e., 1 × 1, 2 × 2, 3 × 3, 4 × 4, 5 × 5, 6 × 6, 7 × 7, 8 × 8, 9 × 9, 10 × 10, 11 × 11, 12 × 12, 13 × 13, 14 × 14, and 15 × 15 m) were generated and tested by applying uniaxial compressive tests.

In this study, the failure criterion is satisfied when the axial pressure exceeds the maximum contact force between particles. The tensile and shear strength between two particles can be calculated by using

$$\overline{\sigma}^{\max} = \frac{-\overline{F}^{n}}{A} + \frac{\left|\overline{M}^{s}\right|\overline{R}}{I} \tag{6}$$

$$\overline{\tau}^{\max} = \frac{\left|\overline{F}^{s}\right|}{A} + \frac{\left|\overline{M}^{n}\right|\overline{R}}{J} \tag{7}$$

Table 2 Microscopic parameters of simulated specimen after calibration

Micro-parameters	Symbol	Unit	Values
The minimum particle radius	R_{min}	mm	1.0
Ratio of maximum and minimum particle radius	R_{max}/R_{min}	/	1.67
Particle density	ρ	kg/m^3	2800
Particle friction coefficient	μ	/	0.55
Young's modulus of the particle	E	GPa	14.4
Parallel bond radius multiplier	λ	/	1.0
Young's modulus of the parallel bond	$\overline{E}_c$	GPa	14.4
Tensile strength of the parallel bond (mean)	$\sigma_{n\text{-mean}}$	MPa	14.7
Tensile strength of the parallel bond (std deviation)	$\sigma_{n\text{-dev}}$	MPa	3.6
Cohesion of the parallel bond (mean)	$\tau_{s\text{-mean}}$	MPa	9.2
Cohesion of the parallel bond (std deviation)	$\tau_{s\text{- dev}}$	MPa	2.4

where $\overline{F}^n$ and $\overline{F}^s$ are the normal- and shear-directed force exerted by the contact (PBM or SJM), A and I are the area and moment of inertia of the contact cross section, $\overline{\sigma}^{max}$ and $\overline{\tau}^{max}$ are the tensile strength and shear strength, respectively, and J is the polar moment of inertia.

Particle size may also influence the simulation results with different model sizes. Ding et al. (2014) suggested that the effect of particle size R correlates directly with model size L. The macroscopic mechanical properties (strength, modulus, and Poisson's ratio) of a model vary quite significantly when the ratio L/R is relatively small but tend to stabilize when $L/R \geq 50$. Based on this finding, we selected proper-sized particles to ensure $L/R \geq 50$ so that L/R remains as stable as possible.

Estimate of size of representative element volume

Effect of scale and anisotropy on cumulative frequency of acoustic emission events

The relationship between the accumulated frequency and the magnitude of AE events plays an important role in estimating the size of the REV. Figure 6 shows the accumulated number versus the magnitude distribution curve with different model sizes and layer orientations, in which the vertical axis represents the log-transformed value of the accumulated frequency. When the size of the model is less than 10 × 10 m, the accumulated frequencies of AE events in different layer orientations differ significantly. For the same model size (2 × 2 m), the highest accumulated frequency of AE events ($\theta = 0°$, $\log(N) = 3.08$) is more than 30 times that of the lowest accumulated frequency ($\theta = 30°$, $\log(N) = 1.5$). When the model size reaches 9 × 9 m, the highest accumulated frequency of AE events ($\theta = 0°$, $\log(N) = 3.73$) is approximately twice the lowest accumulated frequency ($\theta = 30°$, $\log(N) = 3.42$). From 2 × 2 to 9 × 9 m, the JRM with different layer orientations is anisotropic because of the significantly different accumulated frequencies. When the model size reaches 10 × 10 m or more, the anisotropy caused by the different layer orientations gradually disappears, and the accumulated frequencies of AE events generated in models with different sizes tend to be essentially the same ($\log(N) = 3.75$).

The magnitude of AE events is known to follow a power-law distribution. The Gutenberg–Richter-type relationship is used to examine the AE magnitude (Shivakumar and Rao

Table 3 Geometrical parameters and distribution of joints

Set			Set 1	Set 2	Set 3
Joint characteristics	Density (m^{-1})		1.02	1.34	0.36
	Dip angle (°)	Type	IV	IV	III
		Mean value	86.98	7.10	45.96
		Standard deviation	11.58	4.15	10.77
	Trace length (m)	Type	II	II	III
		Mean value	1.03	1.39	1.21
		Standard deviation	0.31	0.43	0.27
	Spacing (m)	Type	IV	IV	III
		Mean value	0.58	0.42	1.36
		Standard deviation	0.75	0.87	1.28

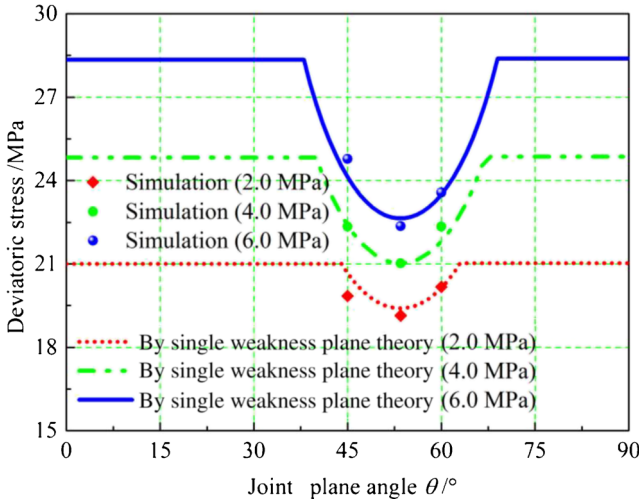

Fig. 4 Comparison of deviatoric stress between numerical results and single plane of weakness theory

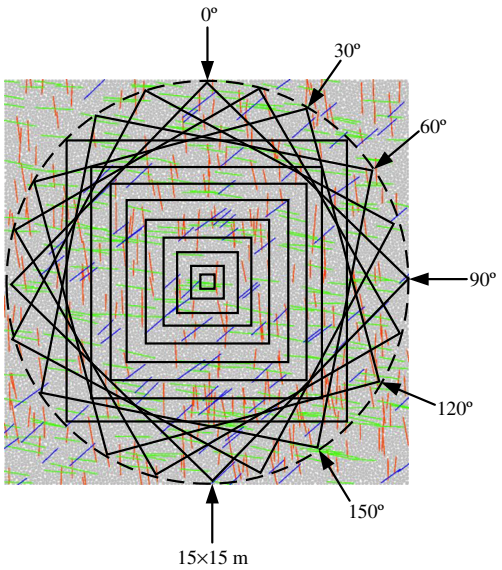

Fig. 5 Schematic diagram of study of scale effect, anisotropy, and the size of the REV

2000). This equation is widely used to investigate AE events in physical experiments or in field tests and is given by

$$\log_{10}(N) = a - bM \tag{8}$$

where N is the accumulated frequency of AE events, M is the magnitude of AE events, a is the mean activity level in the region under investigation, and b is the ratio of the frequency of small events to the frequency of large events. Larger values for b correspond to a larger fraction of large AE events, and vice versa.

To examine the magnitude of an AE event, we fit the curves between logarithmic frequency and AE event magnitude (Fig. 6). When the model size is less than 10 × 10 m, there are usually two sets of values for a and b, which is caused by the anisotropy due to the different layer orientations for smaller model size (Table 5). Similarly, the fit results for a and b also depend strongly on model size. This phenomenon proves that the scale affects the generation of AE events.

However, when the model size reaches 10 × 10 m or more, only one set of values is obtained for a and b for the models with different layer orientations, and a and b vary little with model size. This phenomenon reflects the fact that AE events are very similar to each other when the model size reaches 10 × 10 m or more. When the model size reaches 10 × 10 m or more, b is greater than when the model size is less than 10 × 10 m, which proves that the large-magnitude AE events that occur with high frequency are generated within the model when the model size is relatively large.

Table 4 Micro-properties used in smooth joint (SJ) contact for simulated specimen after calibration

Parameters		Unit	Values
Smooth joint model	Normal stiffness	N/m^3	45.2
	Shear stiffness	N/m^3	38.2
	Tensile strength	MPa	0
	Cohesion	MPa	0
	Friction angle	°	30

Effect of scale and anisotropy on distribution of magnitude of acoustic emission events

In the calculation, the distribution of the magnitude of AE events is also an important factor for estimating the size of the REV. Figure 7 shows the relationship between the magnitude of AE events and the number of AE events for different model sizes. The vertical axis gives the frequency of AE events for different event magnitudes. The frequency of AE events as a function of magnitude follows a normal distribution. Most AE event magnitudes range from − 4.25 to − 3.0 when the model size is 0.1 × 0.1 m (the smallest size). As the model size increases, the magnitude of the AE event also increases. When the model size reaches 1 × 1 m, the AE event magnitude undergoes its most dramatic growth, with the magnitude ranging from − 4.25 to − 3.0. When the model size increases beyond 1 × 1 m, the AE event magnitude continues to fluctuate strongly. When the model size reaches 8 × 8 or 9 × 9 m, however, the increase in AE event magnitude gradually attenuates, and most magnitudes remain stable between − 2.75 and − 1.25. However, the magnitudes also drop below − 2.75 or grow above − 1.25 for some AE events, but the fraction of these AE events is less than 10%.

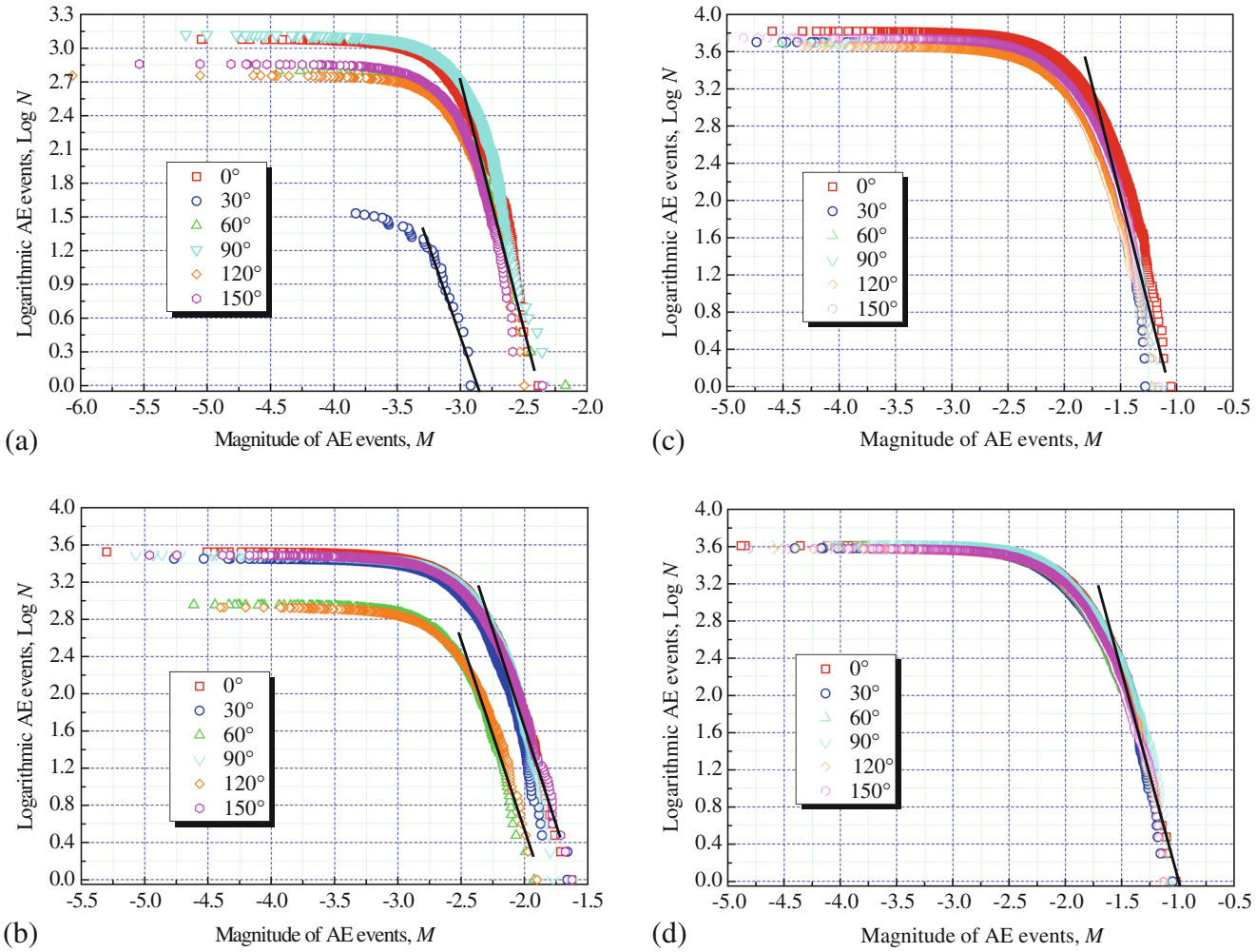

Fig. 6 Relationship between AE event magnitude and logarithmic AE events with different model sizes: **a** 2 × 2 m; **b** 5 × 5 m; **c** 10 × 10 m; **d** 12 × 12 m

Effect of scale and anisotropy acoustic emission events containing the crack number

The other important factor for estimating the size of the REV is the relationship between the number of cracks (*x* coordinate) associated with every AE event and the frequency (*y* coordinate) of the AE event (Fig. 8). These results reveal a negative exponential relationship between the two, which means that, for each AE event, the frequency drops dramatically with increasing number of cracks. For these AE events, the number of cracks ranges from 1 to 3.

Table 6 lists the statistical results of AE events composed of only one crack and of more than ten cracks, and the maximum number of cracks for an AE event. When the model size is very small (i.e., 0.1 × 0.1 and 1 × 1 m), over 90% of AE events are associated with only one crack, and almost no AE event is associated with more than ten cracks. This means that no macro-fracture or fast propagation or coalescence of cracks occurs within the model.

With increasing model size, the fraction of AE events associated with one crack decreases gradually, but the fraction remains near 85% even when the model size reaches 15 × 15 m (the maximum size). The frequency of AE events associated with ten cracks exceeds 250 when the model size reaches 9 × 9 m. This frequency exceeds 260 and the maximum number of cracks associated with a single AE event exceeds 20 when the model size reaches 10 × 10 m. As the model size increases, these two sets of values remain essentially similar and show no further increase. This means that, when the model size reaches 10 × 10 m or more, many cracks within the JRM start to propagate and coalesce, but the parameters of the AE events excited by the cracks remain essentially the same.

Discussion

This paper proposes the use of an independent sub-program to calculate AE events. We apply the moment tensor in the DFN

Table 5 Results of fits for *a* and *b* of accumulated AE events

Model size	Group 1		Group 2	
	a value	*b* value	*a* value	*b* value
0.1 × 0.1 m	− 10.38	1.66	NA	NA
1 × 1 m	− 9.28	2.46	NA	NA
2 × 2 m	− 5.04	2.53	− 4.67	1.79
3 × 3 m	− 4.55	2.74	− 3.79	1.87
4 × 4 m	− 9.50	3.19	− 9.61	2.51
5 × 5 m	− 5.26	3.54	− 6.84	3.73
6 × 6 m	− 2.68	2.57	− 3.87	2.67
7 × 7 m	− 4.29	3.57	NA	NA
8 × 8 m	− 5.06	4.32	− 4.79	3.62
9 × 9 m	− 4.00	3.83	− 3.44	3.03
10 × 10 m	− 5.24	5.04	NA	NA
11 × 11 m	− 4.78	4.72	NA	NA
12 × 12 m	− 4.29	4.96	NA	NA
13 × 13 m	− 3.01	5.02	NA	NA
14 × 14 m	− 4.92	4.88	NA	NA
15 × 15 m	− 4.43	5.10	NA	NA

model and use an algorithm to identify identical AE events. Next, the parameters of the DEM model are calibrated based on physical experiments with intact specimens and the statistical results of joint planes. After calibration, the proposed model is used to investigate the AE characteristics of the JRM. The proposed model has the following advantages:

(1) The proposed calculation is effective and successful for investigating how scale and anisotropy affect the JRM. Once the model is calibrated based on a given set of experiments, it can be used to expand our knowledge to the cases that cannot easily be tested.
(2) The proposed model accounts for the anisotropy and heterogeneity of JRM. With this model, micro-seismic events within the JRM and that are excited by the initiation, propagation, and coalescence of cracks during the loading process can be recorded by using an independent algorithm.

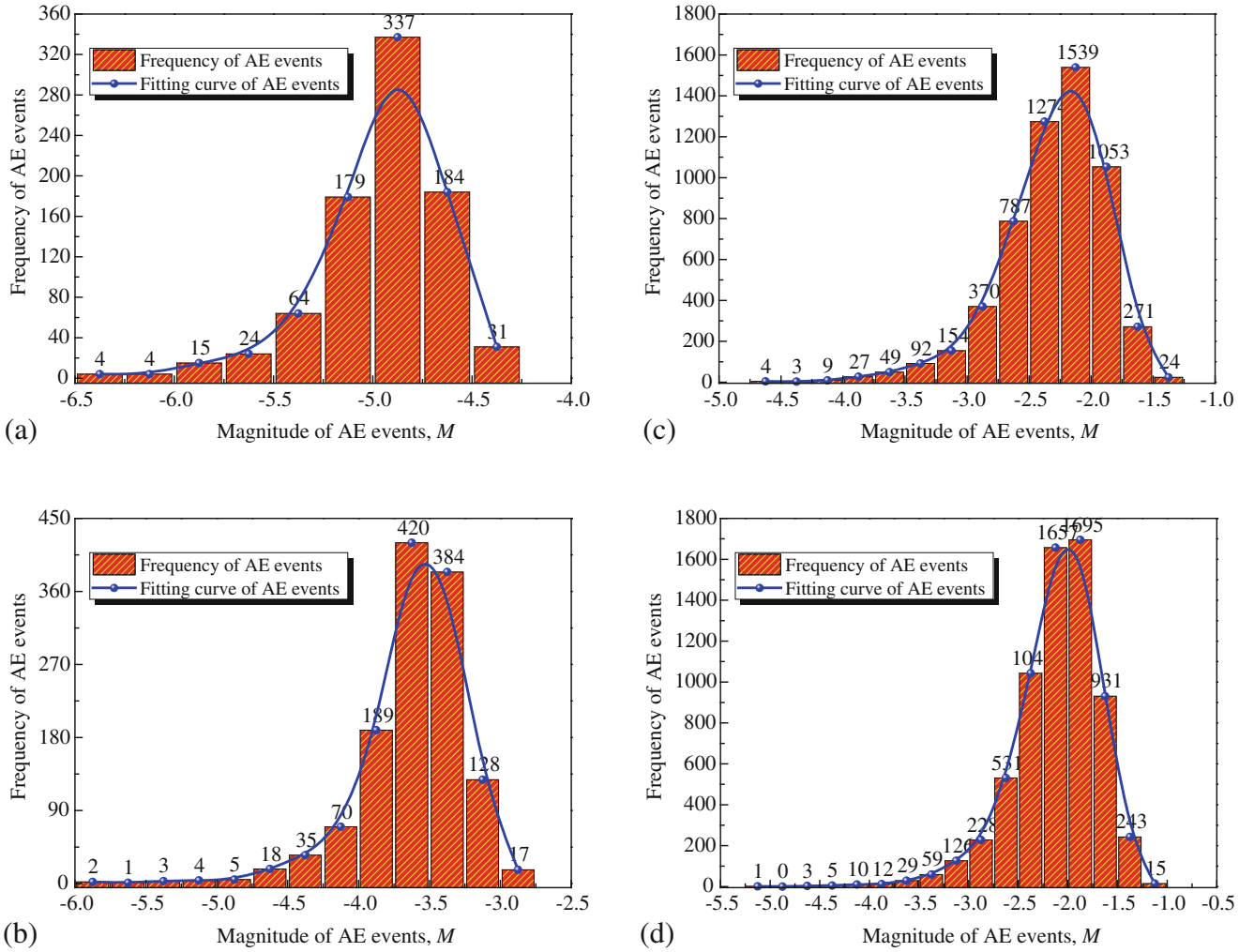

Fig. 7 Relationship between AE event magnitude and number of AE events for various model sizes at $\theta = 0°$: **a** 0.1 × 0.1 m; **b** 1 × 1 m; **c** 8 × 8 m; **d** 10 × 10 m

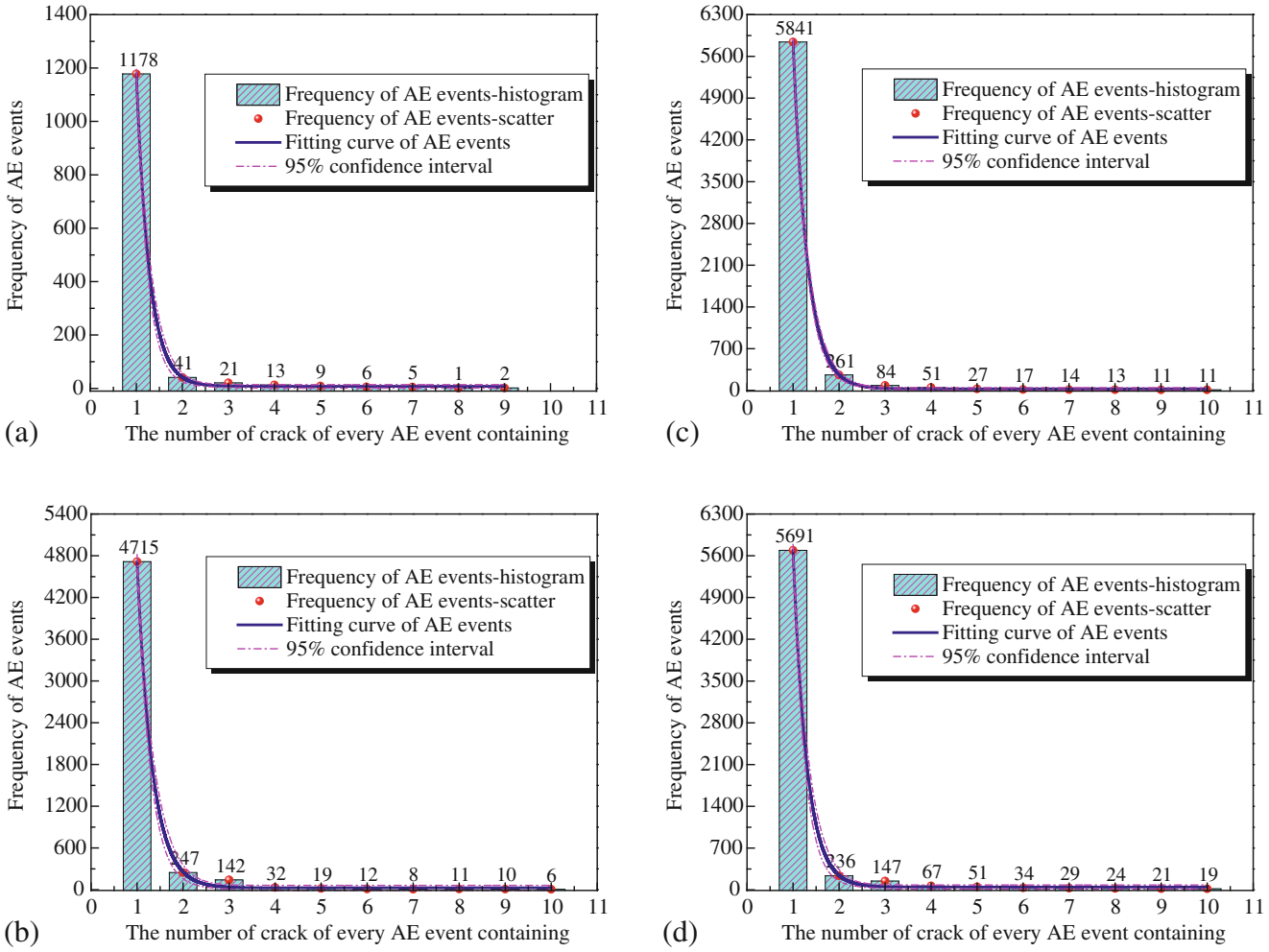

Fig. 8 AE event frequency as a function of the number of cracks for every AE event and for various model sizes at $\theta = 0°$: **a** 1 × 1 m; **b** 9 × 9 m; **c** 10 × 10 m; **d** 15 × 15 m

Table 6 Statistical results of AE events composed of only one crack and more than ten cracks, and maximum number of cracks for an AE event for different model sizes

Model size	The ratio of AE event composed of only one crack (average of different θ) (%)	AE event composed of more than ten cracks (average of different θ)	Maximum crack number of an AE event containing (average of different θ)
0.1 × 0.1 m	93.23	0	7
1 × 1 m	90.27	1	10
2 × 2 m	89.83	2	11
3 × 3 m	88.27	7	14
4 × 4 m	88.16	22	15
5 × 5 m	88.06	35	15
6 × 6 m	87.15	137	19
7 × 7 m	87.12	162	20
8 × 8 m	87.01	228	20
9 × 9 m	86.41	253	19
10 × 10 m	86.11	269	23
11 × 11 m	85.31	271	24
12 × 12 m	85.90	263	23
13 × 13 m	86.00	277	23
14 × 14 m	85.53	251	24
15 × 15 m	85.80	262	24

Figure 9 shows the AE event distribution for various model sizes at $\theta = 0°$ in which yellow dashed lines represent pre-existing joint planes. These results reveal that the JRM contains fewer joint planes when the model size is relatively small (i.e., between 0.1×0.1 and 5×5 m), and evolution of fractures caused by AE events can be clearly seen.

Figure 10 shows the vertical stress versus strain curve, the development of cracks, and AE events with different sizes at $\theta = 0°$. When the model size is 0.1×0.1 m, no pre-existing joint plane exists within the specimen and cracks start to form only when vertical stress rises to 80% of the peak stress. At the same time, AE events

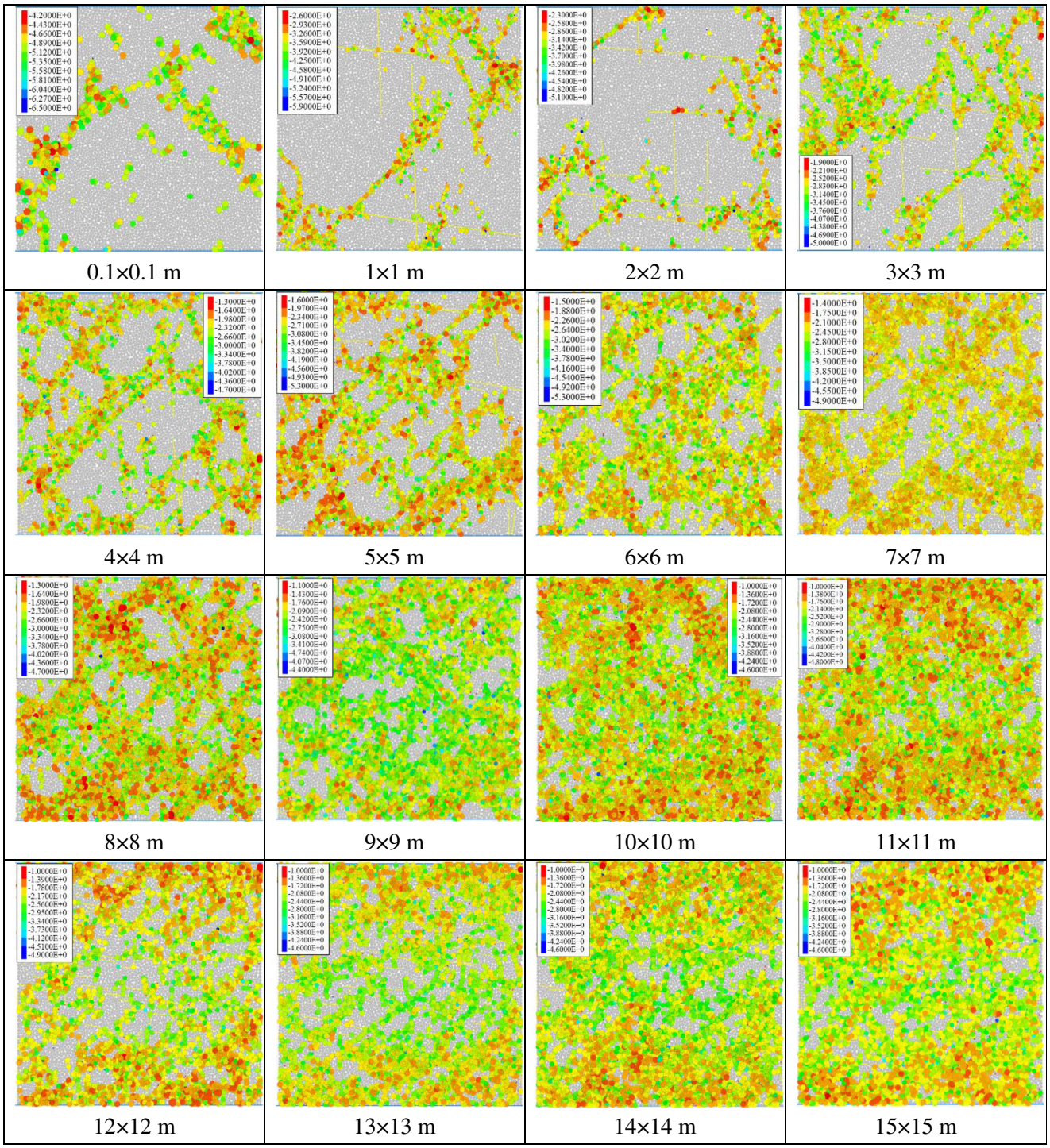

Fig. 9 AE event distribution at $\theta = 0°$ with model size ranging from 0.1×0.1 to 15×15 m

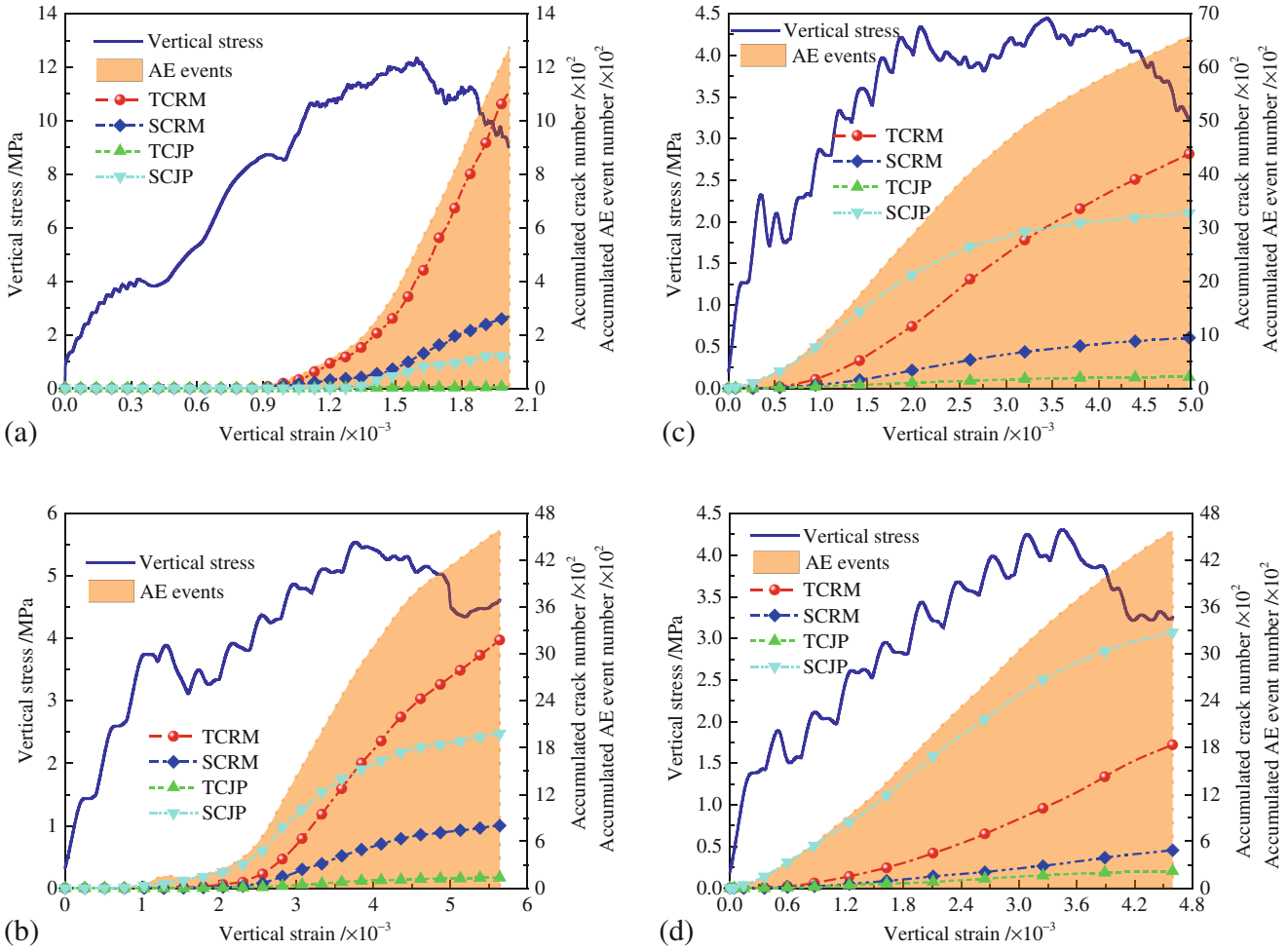

Fig. 10 Vertical stress, accumulated number of cracks, and accumulated number of AE events as a function of vertical strain and for various model sizes at $\theta = 0°$: **a** 1 × 1 m; **b** 7 × 7 m; **c** 10 × 10 m; **d** 13 × 13 m

appear. The threshold for crack initiation and the number of AE events decrease with increasing model size. When the model size reaches 10 × 10 m or more, cracks and AE events initiate at the beginning of the loading process.

It is impossible to capture the characteristics of crack development in the DEM model because each AE event in this model is associated with several different types of cracks, which means that an AE event indicates the magnitude of the signal released by crack initiation during the loading process but does not identify the specimen failure modes.

Note that the stress versus strain curve from the JRM simulation differs slightly from the result obtained from physical experiment. There are perhaps two reasons for this: First, the rock mass was anisotropic or ηετερογενεουσ because of the discontinuous distribution of joint planes in the numerical simulation. Second, the unstable propagation of cracks during the simulation caused fluctuations in the simulated curves.

Conclusions

We propose a calculation to investigate how the scale and anisotropy of AE characteristics affect the JRM. To begin, we study the distribution of joint planes, from which three sets of geometric parameters are obtained and used to generate a DFN. Second, we calibrate the micro-parameters of the rock matrix by using confining pressure tests and the micro-parameters of joint planes based on the single plane of weakness theory. Finally, the validated DEM model is applied in a series of numerical simulations to investigate how scale and anisotropy affect the AE characteristics. The results lead to the following conclusions:

(1) The AE event magnitude follows a power-law distribution for various model sizes. When the model size increases to 10 × 10 m or more, the accumulated frequency of AE events remains stable for different model sizes. A relatively stable linear relationship appears between

frequency and the magnitude of log-transformed AE events (both parameters *a* and *b* vary little).

(2) The AE event frequencies for different AE event magnitudes follow a normal distribution. When the model size attains 10 × 10 m or more, most AE event magnitudes remain quite stable (between − 2.75 and − 1.25).

(3) The AE event frequency as a function of crack number associated with each AE event is a negative exponential, which means that fewer cracks associated with a given AE event correspond to a higher AE event proportion. When the model size increases to 10 × 10 m or more, the AE events with one crack account for about 85% of the total number of AE events, and the frequency of the AE events associated with more than ten cracks exceed 260. Finally, the maximum number of cracks associated with a single AE event exceeds 20. These parameters essentially remain stable.

Based on all these parameters, the size of the REV is determined to be 10 × 10 m. The model proposed herein can support the study of mechanical mechanisms for discontinuities in rock mass and the verification of AE characteristics.

Funding information This research is supported by the Fundamental Research Funds for the Central Universities (2017XKZD06).

References

Andrä H, Combaret N, Dvorkin J, Glatt E, Han J, Kabel M, Keehm Y, Krzikalla F, Lee M, Madonna C, Marsh M, Mukerji T, Saenger EH, Sain R, Saxena N, Ricker S, Wiegmann A, Zhan X (2013) Digital rock physics benchmarks—part i: imaging and segmentation. Comput Geosci-Uk 50:25–32

Bahaaddini M, Sharrock G, Hebblewhite BK (2013) Numerical investigation of the effect of joint geometrical parameters on the mechanical properties of a non-persistent jointed rock mass under uniaxial compression. Comput Geotech 49:206–225

Blum P, Mackay R, Riley MS, Knight JL (2007) Hydraulische modellierung und die ermittlung des repräsentativen elementarvolumens (rev) im kluftgestein. Grundwasser 12:48–65

Cai M, Kaiser PK, Morioka H, Minami M, Maejima T, Tasaka Y, Kurose H (2007) Flac/pfc coupled numerical simulation of AE in large-scale underground excavations. Int J Rock Mech Min 44(4):550–564

Chen W, Konietzky H (2014) Simulation of heterogeneity, creep, damage and lifetime for loaded brittle rocks. Tectonophysics 633:164–175

Cho N, Martin CD, Sego DC (2007) A clumped particle model for rock. Int J Rock Mech Min 44(7):997–1010

Chong Z, Li X, Hou P, Wu Y, Zhang J, Chen T, Liang S (2017) Numerical investigation of bedding plane parameters of transversely isotropic shale. Rock Mech Rock Eng 20(5):1183–1204

Ding X, Zhang L, Zhu H, Zhang Q (2014) Effect of model scale and particle size distribution on pfc3d simulation results. Rock Mech Rock Eng 47(6):2139–2156

Esmaieli K, Hadjigeorgiou J, Grenon M (2010) Estimating geometrical and mechanical rev based on synthetic rock mass models at Brunswick Mine. Int J Rock Mech Min 47(6):915–926

Fan X, Kulatilake PHSW, Chen X (2015) Mechanical behavior of rock-like jointed blocks with multi-non-persistent joints under uniaxial loading: a particle mechanics approach. Eng Geol 190:17–32

Gao F, Stead D, Kang H (2014) Numerical investigation of the scale effect and anisotropy in the strength and deformability of coal. Int J Coal Geol 136:25–37

Hazzard JF, Young, RP (2000) Simulating acoustic emissions in bonded-particle models of rock. 37(5): 867–872

Heinze T, Galvan B, Miller SA (2015) A new method to estimate location and slip of simulated rock failure events. Tectonophysics 651-652: 35–43

Hoek E, Kaiser PK, Bawden WF (1995) Support of underground excavations in hard rock. A. A. Balkema Publishers

Hou P, Gao F, Yang Y, Zhang X, Zhang Z (2016) Effect of the layer orientation on mechanics and energy evolution characteristics of shales under uniaxial loading. Int J Min Sci Technol 26(5):857–862

Huang Y, Yang S, Tian W, Zeng W, Yu L (2016) An experimental study on fracture mechanical behavior of rock-like materials containing two unparallel fissures under uniaxial compression. Acta Mech Sinica-Prc 32(3):442–455

Ivars DM, Pierce ME, Darcel C, Reyes-Montes J, Potyondy DO, Young RP, Cundall PA (2011) The synthetic rock mass approach for jointed rock mass modelling. Int J Rock Mech Min 48(2):219–244

Jaeger JC (1960a) Shear failure of anistropic rocks. Geol Mag 97(01):65

Jaeger JC (1960b) Shear strength of weakness planes in rock. Geol Mag 91(01):65–72

Karacan CÖ (2009) Forecasting gob gas venthole production performances using intelligent computing methods for optimum methane control in longwall coal mines. Int J Coal Geol 79(4):131–144

Karakul H, Ulusay R (2013) Empirical correlations for predicting strength properties of rocks from p-wave velocity under different degrees of saturation. Rock Mech Rock Eng 46(5):981–999

Kovari K, Tisa A, Einstein HH, Franklin JA (1983) Suggested methods for determining the strength of rock materials in triaxial compression: revised version. Int J Rock Mech Min 20(6):283–290

Kulatilake PHSW (1985) Estimating elastic constants and strength of discontinuous rock. J Geotech Eng 111(7):847–864

Kulatilake PHSW, Wang S, Stephansson O (1993a) Effect of finite size joints on the deformability of jointed rock in three dimensions. Int J Rock Mech Min 30(5):479–501

Kulatilake PHSW, Wathugala D, Stephansson O (1993b) Joint network modelling with a validation exercise in Stripa Mine, Sweden. Int J Rock Mech Min 30(5):503–526

Kulatilake PHSW, Chen J, Teng J, Shufang X, Pan G (1996) Discontinuity geometry characterization in a tunnel close to the proposed permanent shiplock area of the three gorges dam site in China. Int Int J Rock Mech Min 33(3):255–277

Kulatilake PHSW, Malama B, Wang J (2001) Physical and particle flow modeling of jointed rock block behavior under uniaxial loading. Int J Rock Mech Min 38(5):641–657

Kulatilake PHSW, Um J, Wang M, Escandon R, Narvaiz J (2003) Stochastic fracture geometry modeling in 3-D including validations for a part of Arrowhead East Tunnel, California, USA. Eng Geol 70(1):131–155

Lisjak A, Liu Q, Zhao Q, Mahabadi OK, Grasselli G (2013) Numerical simulation of acoustic emission in brittle rocks by two-dimensional finite-discrete element analysis. Geophys J Int 195(1):423–443

Liu J, Li Y, Xu S, Xu S, Jin C, Liu Z (2015) Moment tensor analysis of acoustic emission for cracking mechanisms in rock with a pre-cut circular hole under uniaxial compression. Eng Fract Mech 135:206–218

Mahdevari S, Maarefvand P (2016) An investigation into the effects of block size distribution function on the strength of bimrocks based on large-scale laboratory tests. Arab J Geosci 9(7)

Mclamore R, Gray KE (1967) The mechanical behavior of anisotropic sedimentary rocks. J Eng Ind:62–73

Mehranpour MH, Kulatilake PHSW (2016) Comparison of six major intact rock failure criteria using a particle flow approach under true-triaxial stress condition. Geomech Geophys Geo-Energy Geo-Resour 2(4):203–229

Mehranpour MH, Kulatilake PHSW (2017) Improvements for the smooth joint contact model of the particle flow code and its applications. Comput Geotech 87:163–177

Mehranpour MH, Kulatilake PHSW, Ma X, He M (2018) Development of new three-dimensional rock mass strength criteria. Rock Mech Rock Eng 51(11):3537–3561

Min K, Jing L, Stephansson O (2004) Determining the equivalent permeability tensor for fractured rock masses using a stochastic rev approach: method and application to the field data from Sellafield, UK. Hydrogeol J 12(5):497–510

Moriya H, Naoi M, Nakatani M, Aswegen GV, Murakami O, Kgarume T, Ward AK, Durrheim RJ, Philipp J, Yabe Y, Kawakata H, Ogasawara H (2015) Delineation of large localized damage structures forming ahead of an active mining front by using advanced acoustic emission mapping techniques. Int J Rock Mech Min 79:157–165

Pierce M, Cundall R, Potyondy D, Ivars DM (2007) A synthetic rock mass model for jointed rock. In: Eberhardt E, Stead D, Morrison T (eds) Proceedings and Monographs in Engineering, Water and Earth Sciences, pp 341–349

Potyondy DO, Cundall PA (2004) A bonded-particle model for rock. Int J Rock Mech Min 41(8):1329–1364

Shi X, Cai W, Meng Y, Li G, Wen K, Zhang Y (2016) Weakening laws of rock uniaxial compressive strength with consideration of water content and rock porosity. Arab J Geosci 9(5)

Shivakumar K, Rao MVMS (2000) Application of fractals to the study of rock fracture and rockburst-associated seismicity. New Delhi. Application of Fractals in Earth Sciences. AA Balkema, USA/Oxford, and IBH Pub. Co., pp 171–188

Shukla R, Ranjith PG, Choi SK, Haque A, Yellishetty M, Hong L (2013) Mechanical behaviour of reservoir rock under brine saturation. Rock Mech Rock Eng 46(1):83–93

Tang CA, Liu H, Lee P, Tsui Y, Tham LG (2000a) Numerical studies of the influence of microstructure on rock failure in uniaxial compression-part i: effect of heterogeneity. Int J Rock Mech Min 37(4):555–569

Tang CA, Tham LG, Lee P, Tsui Y, Liu H (2000b) Numerical studies of the influence of microstructure on rock failure in uniaxial compression-part ii: constraint, slenderness and size effect. Int J Rock Mech Min 37(4):571–583

Vásárhelyi B, Kovács D (2017) Empirical methods of calculating the mechanical parameters of the rock mass. Period Polytech-Civ 61(1):39

Wang P, Yang T, Xu T, Cai M, Li C (2016) Numerical analysis on scale effect of elasticity, strength and failure patterns of jointed rock masses. Geosci J 20(4):539–549

Wu Q, Kulatilake PHSW (2012) Application of equivalent continuum and discontinuum stress analyses in three-dimensions to investigate stability of a rock tunnel in a dam site in China. Comput Geotech 46:48–68

Wu S, Xu X (2016) A study of three intrinsic problems of the classic discrete element method using flat-joint model. Rock Mech Rock Eng 49(5):1813–1830

Xue L, Qin S, Sun Q, Wang Y, Lee LM, Li W (2014) A study on crack damage stress thresholds of different rock types based on uniaxial compression tests. Rock Mech Rock Eng 47(4):1183–1195

Yang XX, Qiao WG (2018) Numerical investigation of the shear behavior of granite materials containing discontinuous joints by utilizing the flat-joint model. Comput Geotech 104(12):69–80

Younessi A, Rasouli V (2010) A fracture sliding potential index for wellbore stability analysis. Int J Rock Mech Min 47(6):927–939

Zhang L (2010) Estimating the strength of jointed rock masses. Rock Mech Rock Eng 43(4):391–402

Zhao XG, Wang J, Cai M, Cheng C, Ma LK, Su R, Zhao F, Li DJ (2014) Influence of unloading rate on the strainburst characteristics of Beishan granite under true-triaxial unloading conditions. Rock Mech Rock Eng 47(2):467–483

Zhao Q, Tisato N, Grasselli G, Mahabadi OK, Lisjak A, Liu Q (2015) Influence of in-situ stress variations on acoustic emissions: a numerical study. Geophys J Int 203(2):1246–1252